GDCh

Research Articles

Angewandte
Chemie
International Edition
www.angewandte.org

Li-Ion Batteries | Hot Paper

Long-Range Cationic Disordering Induces two Distinct Degradation Pathways in Co-Free Ni-Rich Layered Cathodes

Weibo Hua[+],* Jilu Zhang[+], Suning Wang[+], Yi Cheng, Hang Li, Jochi Tseng, Zhonghua Wu, Chong-Heng Shen, Oleksandr Dolotko, Hao Liu, Sung-Fu Hung, Wei Tang,* Mingtao Li, Michael Knapp, Helmut Ehrenberg, Sylvio Indris,* and Xiaodong Guo*

Abstract: Ni-rich layered oxides are one of the most attractive cathode materials in high-energy-density lithium-ion batteries, their degradation mechanisms are still not completely elucidated. Herein, we report a strong dependence of degradation pathways on the long-range cationic disordering of Co-free Ni-rich $Li_{1-m}(Ni_{0.94}Al_{0.06})_{1+m}O_2$ (NA). Interestingly, a disordered layered phase with lattice mismatch can be easily formed in the near-surface region of NA particles with very low cation disorder (NA-LCD, $m \leq 0.06$) over electrochemical cycling, while the layered structure is basically maintained in the core of particles forming a "core–shell" structure. Such surface reconstruction triggers a rapid capacity decay during the first 100 cycles between 2.7 and 4.3 V at 1 C or 3 C. On the contrary, the local lattice distortions are gradually accumulated throughout the whole NA particles with higher degrees of cation disorder (NA-HCD, $0.06 \leq m \leq 0.15$) that lead to a slow capacity decay upon cycling.

Introduction

Lithium-ion batteries (LIBs) have become an indispensable part of our daily life, powering portable electronic devices like laptops and electrical vehicles (EVs) that have driven the advances in the field of energy storage.[1] Their significance was recognized by the award of the 2019 Nobel Prize in Chemistry to pioneering scientists working in this area.[2] In the development of LIBs, high-performance cathode materials are usually the central bottleneck because they limit the energy density and dominate the cost of LIB cells.[3] Ni-rich layered oxides ($LiNi_xCo_yMn_{1-x-y}O_2$, $x \geq 0.6$) are very attractive candidates as cathode materials for EV batteries due to their high specific capacity and low material cost.[4] For instance, Tesla uses $LiNi_{0.8}Co_{0.15}Al_{0.05}O_2$ (NCA) cathode materials in the EV models S and X.[5] It is widely expected that LIBs require a further increase in capacity to achieve a long driving range beyond 500 km and an even lower price of EV battery packs.[6] For this reason, tremendous efforts have recently been made to develop highly Ni-rich layered oxide cathode materials, where the Ni concentration is higher than 90 % and the gravimetric capacity is beyond 210 mAh g^{-1}.[7]

Despite these advantages, high-Ni-content layered cathode materials are susceptible to chemical and mechanical

---

[*] Prof. W. Hua,[+] J. Zhang,[+] Dr. S. Wang,[+] Prof. W. Tang, Prof. M. Li
School of Chemical Engineering and Technology, Xi'an Jiaotong University
No.28, West Xianning Road, Xi'an, Shaanxi 710049 (China)
E-mail: weibo.hua@xjtu.edu.cn
tangw2018@xjtu.edu.cn

Prof. W. Hua,[+] Dr. S. Wang,[+] Dr. H. Li, Dr. O. Dolotko, H. Liu, Dr. M. Knapp, Prof. H. Ehrenberg, Dr. S. Indris
Institute for Applied Materials (IAM), Karlsruhe Institute of Technology (KIT)
Hermann-von-Helmholtz-Platz 1, 76344 Eggenstein-Leopoldshafen (Germany)
E-mail: sylvio.indris@kit.edu

Y. Cheng, Dr. S.-F. Hung
Department of Applied Chemistry, National Yang Ming Chiao Tung University
Hsinchu 30010 (Taiwan)

Dr. J. Tseng
Diffraction and Scattering Division, Japan Synchrotron Radiation Research Institute (JASRI)
1-1-1, Kouto, Sayo-cho, Sayo-gun, Hyogo 679-5198 (Japan)

Prof. Z. Wu
Beijing Synchrotron Radiation Facility, Institute of High Energy Physics, Chinese Academy of Sciences
100049 Beijing (China)

Dr. C.-H. Shen
Contemporary Amperex Technology Co.
Ningde, 352100 (China)

Prof. X. Guo
School of Chemical Engineering, Sichuan University
No. 24 South Section 1, Yihuan Road, 610065, Chengdu (China)
E-mail: xiaodong2009@scu.edu.cn

[+] These authors contributed equally to this work.

degradations that result in inferior cycling and thermal stability.[8] Therefore, exploring the nature of the structural degradation and capacity fading mechanisms of Ni-rich cathodes has become an intensively discussed topic in both academic science and industrial research.[4a] Several possible mechanisms were proposed, e.g. phase transition from the initially layered structure to spinel and/or rock-salt-like structure,[9] surface reconstruction caused by the release of Li/O[1a, 10] and strain-induced anisotropic intragranular cracking.[11] In addition, the transition metal relative ratios in Ni-rich cathodes strongly affect the electrochemical properties, e.g. high cobalt content is beneficial for improving the rate capability and structural stability.[12] Eliminating cobalt from Ni-rich layered oxides is highly desired owing to the toxic nature of cobalt.[7b,13] As a matter of fact, the electrochemical performances of Ni-rich cathodes are also closely tied to the Li/Ni cation mixing in the layered structure because a large amount of Ni cations in Li layer could greatly increase the kinetic barrier for Li-ion diffusion.[14] Unfortunately, we do not yet have a clear understanding of how the long-range cationic disordering influences degradation pathways of Co-free Ni-rich materials during prolonged cycling up to now.

In this study, Co-free Ni-rich layered $Li_{1-m}(Ni_{0.94}Al_{0.06})_{1+m}O_2$ (NA, m denotes some Ni/Al excesses) oxides with varying degrees of cation disorder were synthesized using a facile solid-state reaction method. NA-HCD cathodes exhibit a lower capacity (around 200 $mAhg^{-1}$ at 0.1 C) compared to NA-LCD cathodes (about 216 $mAhg^{-1}$) because of lack of the plateau at ≈ 4.2 V versus Li. Interestingly, there is only a small decrease in the capacity of NA-HCD cathodes during cycling, maintaining about 78% of their initial capacity after 300 cycles at 1 C. In contrast, NA-LCD electrodes experience a fast capacity fading during the first 100 cycles and a small reduction in capacity in the following cycles. Various characterization techniques were used to identify the origin of the fatigue process of these materials. *In situ* XRD measurements were conducted to investigate the difference in the electrochemical behaviors of NA cathodes during the first cycle. Ex situ XRD combined with transmission electron microscopy (TEM) techniques were used to show the correlation between the long-range cationic disordering and degradation pathways of NA cathodes. The rapid capacity fading of NA-LCD cathodes for the first 100 cycles is attributable to the formation of a disordered surface reconstruction layer with serious lattice mismatch. The layered structure of bulk NA-LCD cathodes does not change significantly after extended cycling. In contrast, lattice distortions are gradually generated within the whole NA-HCD crystallites during cycling. Such cation disorder dependent degradation process has never been reported before. This work could open up a new avenue for developing an effective approach to eliminate the degradation process.

Results and Discussion

A series of $Li_{1-m}(Ni_{0.94}Al_{0.06})_{1+m}O_2$ (NA, $0.01 \leq m \leq 0.15$) compounds with different degrees of cation mixing were synthesized via a coprecipitation route followed by a calcination process, details of this synthesis process are in the Supporting Information. The hydroxide coprecipitation method was used to fabricate spherical hydroxide precursors (i.e. $Ni_{0.94}Al_{0.06}(OH)_{2.06}$), as shown in Figure S1–S3 Supporting Information. *In situ* high-temperature X-ray diffraction (HTXRD) experiments were first carried out to explore the changes from the long-range cationic disordering to ordering during the synthesis of NA oxides. Figure 1b shows the *in situ* HTXRD patterns of a mixture of $Ni_{0.94}Al_{0.06}(OH)_{2.06}$ precursor and $LiOH \cdot H_2O$ during heating in air (from 25°C to 800°C). Evidently, both $Ni_{0.94}Al_{0.06}(OH)_{2.06}$ ($P\bar{3}m1$) and $LiOH \cdot H_2O$ can be observed in the HTXRD patterns at lower temperatures (< 100°C). When the temperature raises to around 500°C, the reflections in the HTXRD patterns belonging to $Ni_{0.94}Al_{0.06}(OH)_{2.06}$ disappear and a new set of reflections (e.g. at 37° and 43°) appears. The absence of 003 reflection is indicative of the formation of highly cation disordered layered $Li_{1-m}(Ni_{0.94}Al_{0.06})_{1+m}O_2$ ($R\bar{3}m$). The 003 reflection at 18.3° progressively emerges when the temperature increases to around 650°C, which suggests that Li and Ni/Al cations are successively separated into the Li layer and TM layer in the layered structure. Rietveld refinement results are shown in Figure 1c. It is clear that the content of TM ions on the Li sites is decreased from ≈ 0.33 at 500°C to ≈ 0.02 at 800°C. On the basis of the *in situ* HTXRD results, the heating temperatures for lithiation reactions were chosen as 600, 625, 650, 675, 700, 725 and 750°C, respectively, for 12 h in O_2 (Figure 1a). Correspondingly, the obtained samples are labelled as NA-600, NA-625, NA-650, NA-675, NA-700, NA-725, and NA-750, respectively. High-resolution synchrotron-based X-ray diffraction (SXRD) and Rietveld refinement (Figure S5, Table S1, Supporting Information) were performed on the pristine NA materials (Figure 1d). The main reflections in the SXRD patterns of NA-600 and NA-625 can be assigned according to a rhombohedral layered phase ($R\bar{3}m$). A low level of Li_2CO_3 impurities can be found in both NA-600 and NA-625, suggesting that a certain amount of Li source was not inserted into the layered structure during high-temperature lithiation reaction. All the samples obtained at higher temperatures (≥ 650°C) are found to be a single layered phase ($R\bar{3}m$). As the heating temperature increases, an increase in reflection splitting of the 006/012 and 018/110 doublets suggests the enlargement of lattice distortion of the cubic-close packed (ccp) oxygen framework along the $[111]_{RS}$ orientation (RS denotes a cubic rock-salt structure phase ($Fm\bar{3}m$)).[15] The integrated intensity ratio of 003 to 104 reflections (I_{003}/I_{104}) increases with increasing temperature. Accordingly, the occupancy of transition metal (TM) ions in Li layer decreases obviously from ≈ 15% for NA-600 to ≈ 1% for NA-750 (Table S2–S8, Supporting Information).

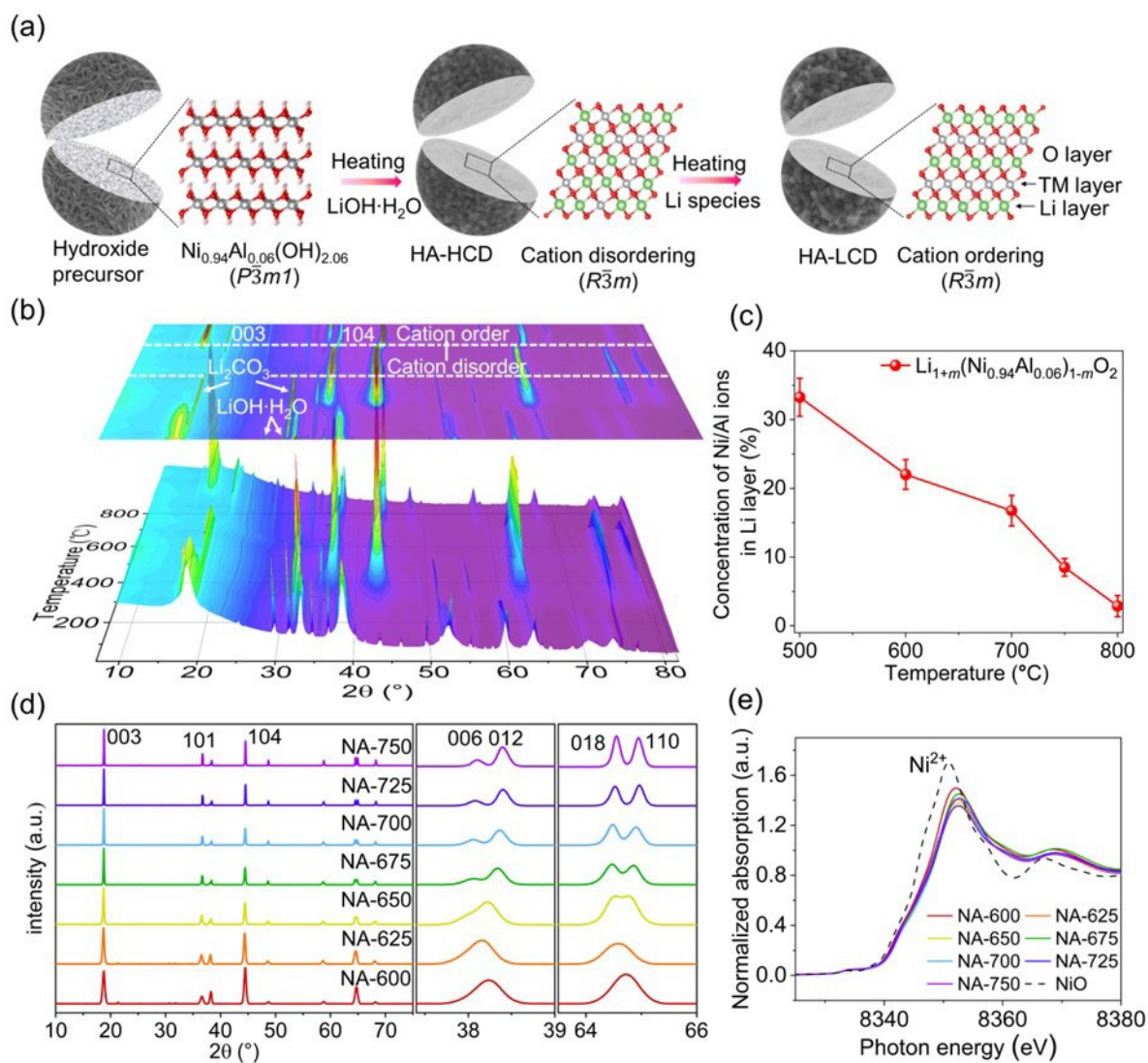The Ni K-edge X-ray absorption near edge structure (XANES) region of XAS spectra shows that the Ni

Figure 1. Structural changes of Ni-rich oxides. a) schematic illustration of a cationic disorder-order transition during synthesis of NA oxides; b) *in situ* HTSRD patterns of a mixture of $Ni_{0.94}Al_{0.06}(OH)_{2.06}$ precursor and $LiOH \cdot H_2O$ during calcination; c) the corresponding changes in the concentration of TM ions in the Li layer; d) SXRD patterns and e) Ni K-edge XANES spectra of NA samples heated to different temperatures.

oxidation state is predominantly $+3$ for NA oxides, as shown in Figure 1e. Two peaks between 1.0 and 3.5 Å are visible in the extended X-ray absorption fine structure (EXAFS) spectra and atomic pair distribution function (PDF) analysis of the samples (Figure 2a–c), corresponding to the Ni–O and Ni–TM interatomic interactions. Note that the Fourier transform (FT) *R*-profiles in the EXAFS spectra are not phase-corrected, leading to a lower peak position of around 0.3 Å compared with their real bond length and the PDF peaks. ^7Li NMR spectroscopy experiments were carried out to investigate the coordination environments of the Li ions in the oxides. A narrow peak at 0 ppm likely stems from diamagnetic impurities such as LiOH and/or Li_2CO_3.[16] The NMR spectrum of NA-600 is dominated by a broad peak at around 705 ppm, which is a feature of $LiNiO_2$ where the local Li environment includes 12 Ni^{3+} (electron configuration $3d^7$) next-nearest neighbours, 6 of them linked

to Li via $\approx 90°$ oxygen bonds and six of them connected to Li via $\approx 180°$ oxygen bonds.[17] Interestingly, an additional peak at about 527 ppm in NA-600 is present, which might reveal a certain amount of Li in the TM layers possibly with mixed paramagnetic Ni^{3+} and diamagnetic Ni^{4+} ($3d^6$) neighbours, which is consistent with the previous studies.[16a] When the temperature is increased above 650 °C, the width of the peak at 705 ppm gradually decreases and the peak at 527 ppm becomes smaller, as shown in Figure 2d, confirming a reduced degree of Li/Ni cation mixing. The high-resolution TEM (HRTEM) image (Figure 2e) of NA-600 displays clear lattice fringes with an average *d*-spacing of 0.47 nm in the selected region (I) of crystallites, which can be indexed to the (003) plane of the trigonal layered structure ($R\bar{3}m$). Obviously, a disordered layered phase with high degree of cation mixing (region II) has grown epitaxially along the [100] direction of ordered layered phase. No such disordered
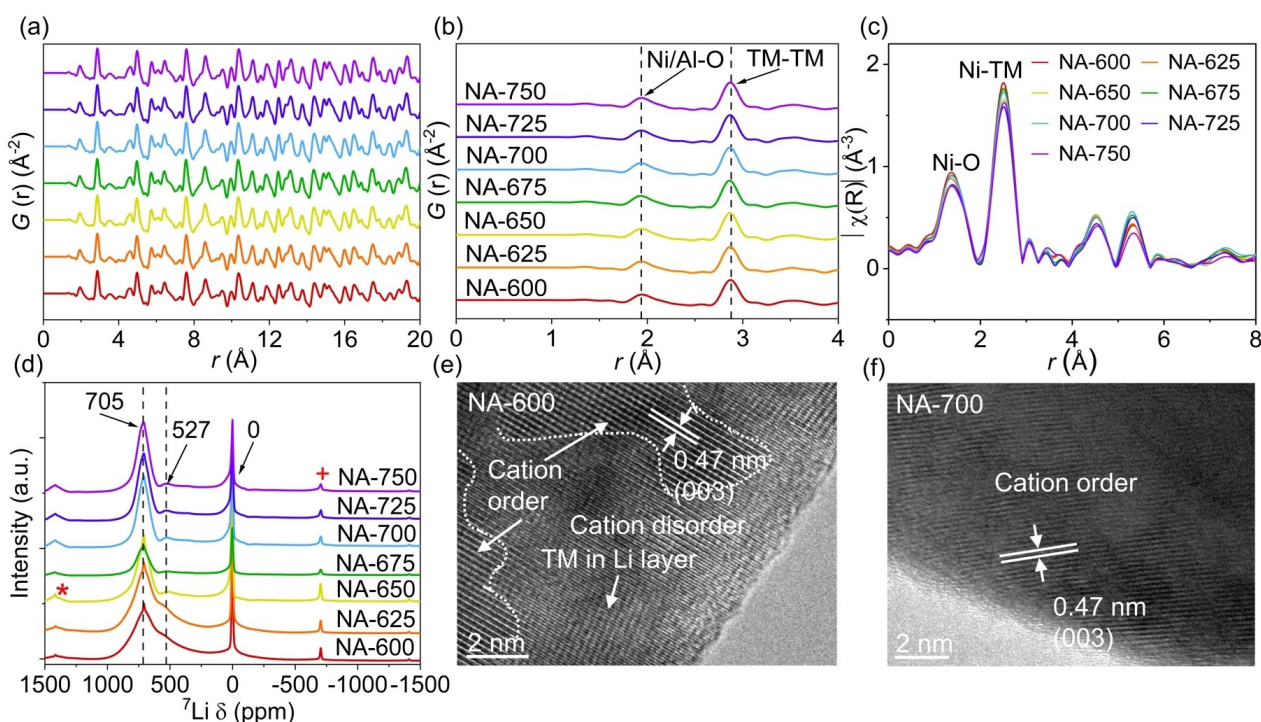
Figure 2. Long-range cationic disordering of Ni-rich oxides. a), b) PDF analysis, c) Ni R-space EXAFS spectra and d) ^{7}Li MAS NMR spectra of NA oxides obtained at various temperatures, HRTEM images of e) NA-600 and f) NA-700. Spinning sidebands are marked with an asterisk and a plus in figure d.

phase can be discovered in the primary crystals of NA-700 (Figure 2f), revealing a gradual cationic disorder to order structural transition as a consequence of Li/O incorporation at high temperature, see Figure S8.

The morphology of NA materials does not change substantially after high-temperature lithiation reaction, as confirmed by the scanning electron microscopy (SEM) images (Figure 3 and Figure S9, Supporting Information). The NA oxides are composed of micrometre-sized (≈ 10 μm) spherical agglomerates that consist of smaller primary particles. Interestingly, the average size of primary particles is increased exponentially with increasing temperature (Figure S10), from ≈ 180 nm for NA-600 to ≈ 710 nm for NA-750. The growth of primary crystals is in good agreement with the literature.[15]

To explore the local structural features that are present at the transition state from cationic disordered to ordered layered structure, a large-area view of a NA-600 particle is shown in Figure 4a. Encouragingly, the disordered and ordered layered structures are always coexisting coherently within a single primary particle, revealing that these two structurally compatible phases are coherently grown during high-temperature lithiation reaction. The inverse fast Fourier transformed (IFFT) TEM image (Figure 4b) displays that a certain amount of TM migrates from TM layer to Li layer in the near-surface region (I) and thus contributing to the generation of the disordered phase. The region (III) (Figure 4d) is attributed to the pure ordered layered phases, as confirmed by the fast-Fourier-transformation (FFT) analysis (Figure 4h). Surprisingly, the ordered layered phase

with two different crystallographic orientations is observed as depicted in Figure 4c and e, forming intergrowths of structurally ordered layered structure. Such overlapping domains with two ordered layered phases can also be misinterpreted by a cubic spinel phase ($Fd\bar{3}m$), as seen previously for LiMn$_2$O$_4$[18] and LiNi$_{0.5}$Mn$_{1.5}$O$_4$.[3a]

In order to unveil the influence of long-range cation disorder on the electrochemical properties of as-synthesized cathode materials, electrochemical measurements were performed on CR2032-type coin cells between 2.7 and 4.3 V at 25°C. Figure 5a exhibits the first charge–discharge potential curves of the NA electrodes at a current density of 0.1 C (1 C = 280 mA g^{-1}). The initial charge/discharge voltage plateaus at approximately 4.2 V of NA-600, NA-625 and NA-650 cathodes are shorter than those of the other cathodes, which is consistent with the reduction of redox peak at ≈ 4.2 V in their differential capacity (dQ/dV) curves (Figure 5b). The initial charge capacities of NA-600, NA-625 and NA650 cathodes are 177, 188 and 197 mAh g^{-1}, respectively, which are smaller than for the other cathodes (211 mAh g^{-1}). All electrodes deliver a similar first-cycle coulombic efficiency, i.e. about 88%. The low capacity of NA-600 and NA-625 electrodes is ascribed to the relatively high content of cation mixing (approximately 10%) that would increase the activation energy for Li diffusion along the *ab* planes to a certain extent.[19] Generally, the dQ/dV peaks of Ni-rich cathodes (Ni ≥ 80%) are in accordance with a sequence of first-order phase transformations during lithiation and delithiation processes,[20] i.e. H1 (pristine electrode)$\rightleftharpoons$M$\rightleftharpoons$H2$\rightleftharpoons$H3, where H represents a hexagonal
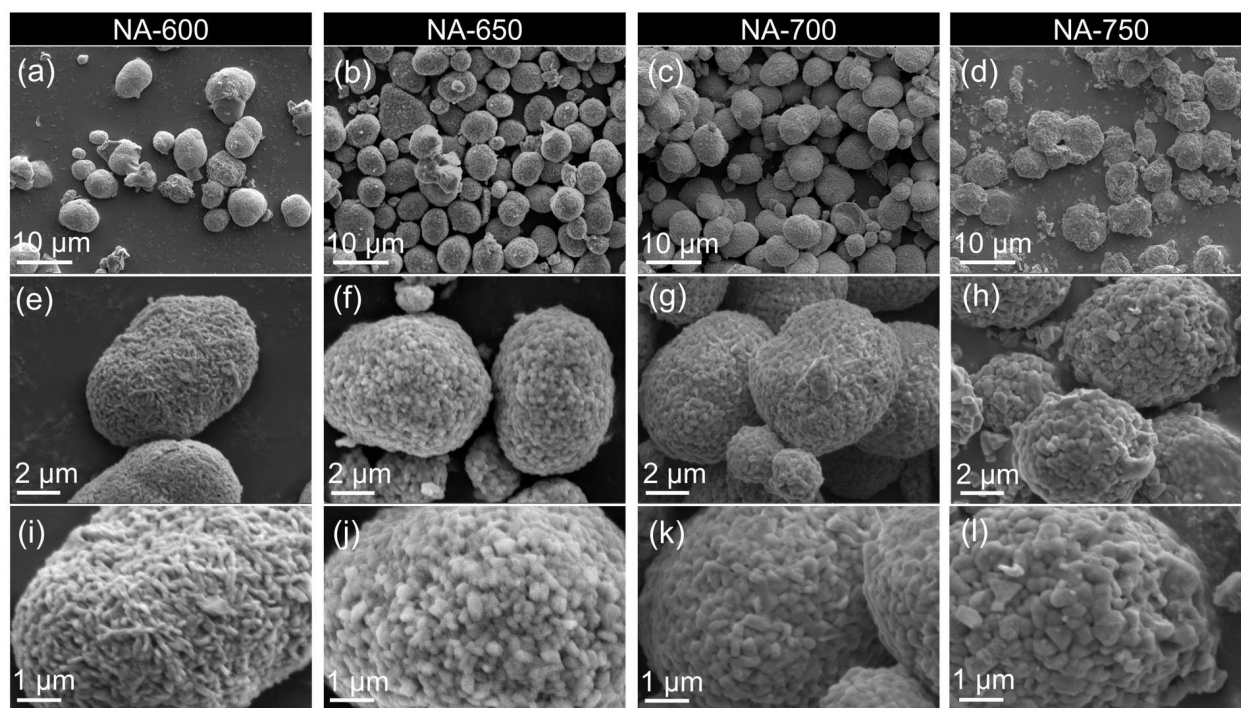
Figure 3. Morphological changes of Ni-rich oxides. SEM images of a), e), i) NA-600, b), f), j) NA-650, c), g), k) NA-700 and d), h), l) NA-750.

phase and M denotes a monoclinic phase.[9] The dQ/dV peaks at ≈4.2 V become sharper as the temperature increases to 750 °C (Figure 4c–i), illustrating a high reactivity of NA-LCD cathodes in the high-voltage regime.

The high-rate capabilities of the NA electrodes are described in Figure 6a, and the NA-675 cathode delivers the best rate performance. The discharge capacities of the NA-675 electrode at 0.1, 1, 5 and 10 C are 221, 195, 178, and 169 mAh g^{-1}, respectively, which are higher than those of the other cathodes (Figure 6a) and most reported values for high-Ni-content cathodes (Ni6Co2Mn2,[21] Ni8Co1Mn1,[22] Ni9Co1,[23] Ni91Co9,[24] Ni93Al7,[25] Ni95Al5,[25] Ni97Al3[25]) (Figure 6b). After ultra-high rate cycling, the discharge capacities of NA-600, NA-625, NA-650, NA-675, and NA-700 electrodes at 0.1 C are almost identical to their initial capacity, demonstrating excellent reversibility. A low capacity of about 130 mAh g^{-1} at 0.1 C after high-rate cycling in both NA-725 and NA-750 cathodes indicates a severe structural degradation. In order to determine the long-term cycling performance of NA cathodes, the Li/NA cells were cycled at high current densities of 1 C (Figure 6e) or 3 C (Figure 6c and Figure S11, Supporting Information). The NA-650 electrode demonstrates an excellent capacity retention of 69 % after 500 cycles at 3 C. The discharge capacities of NA-700, NA-725 and NA-750 cathodes show a significant attenuation after 100 cycles at both 1 C and 3 C. Specifically, the capacity retentions of NA-700, NA-725, and NA-750 cathodes after 100 cycles at 1 C are 58, 39 and 51 %, respectively, which are lower than those of NA-600, NA-625, and NA-650 cathodes (84, 83 and 96 %). The satisfactory cycling performance of NA-600, NA-625 and NA-650 cathodes demonstrates that a certain amount of cation

mixing in Ni-rich cathodes is beneficial for the improvement of their cycling stability. In other words, the increased cationic cation mixing is not the main source of capacity fade and structural fatigue of Ni-rich cathode materials, as already observed in previous studies.[1b]

To decipher the underlying mechanism in the various electrochemical features of the NA cathodes, *in situ* XRD experiments were carried out on the NA-625, NA-650, NA-675, and NA-700 electrodes. Figure 7a–d exhibits the contour profiles of the evolution of 003, 104, 018, and 110 reflections for four cathodes during the first cycle. The three-dimensional (3D) maps of the evolution of 003 reflection during the first charge–discharge processes are shown in Figure 7e–h, which illustrates clearly the structural change. In sharp contrast to the *in situ* XRD patterns of pure layered LiNiO$_2$ cathode,[9,20] which reveals several reflection splittings during the first cycle, all reflections of NA cathodes show continuous shifts without the occurrence of new reflections. As a result, the four cathodes with different amount of long-range cation mixing display a solid solution reaction mechanism during the Li-ion intercalation–deintercalation process. The absence of phase transitions in NA cathodes upon cycling can be interpreted by the lack of long-range Li/vacancy ordering as a consequence of randomly distributed Ni and Al ions in the TM layer.[26] The positional changes in the 003 reflection of NA-625 and NA-650 electrodes are smaller than those of NA-675 and NA-700 electrodes, revealing that more Li-ions are extracted from or inserted into the layered structure of NA-675 and NA-700 (i.e. higher capacity).

The *in situ* XRD patterns were fitted according to a single layered phase ($R\bar{3}m$), the resultant lattice parameters
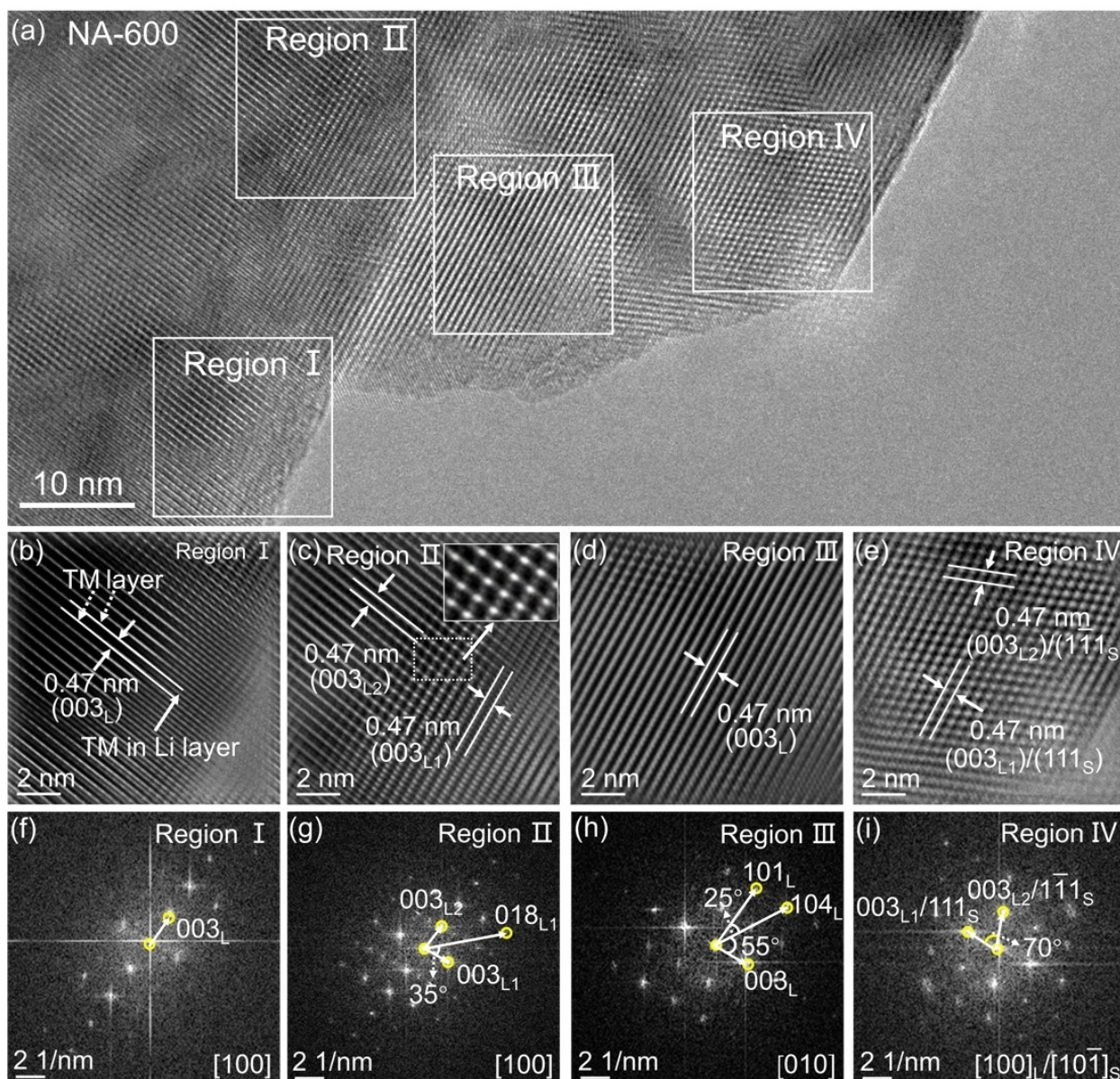
Figure 4. Visualization of long-range cationic disordering within a single particle. a) HRTEM image of NA-600, IFFT-TEM images of selected region (b) I, (c) II, (d) III and (e) IV in figure (a), and corresponding FFT patterns (f–i). L1 and L2 represent layered phase Nr. 1 and Nr. 2, respectively; S means cubic spinel phase.

of NA cathodes are shown in Figure 8. The changes in lattice parameters of these four electrodes are generally similar. Upon de-lithiation, the lattice parameter a of the layered phase progressively declines (Figure 8a), parameter c increases firstly and then decreases massively (Figure 8b). Noticeably, the lattice parameter c of NA-625 and NA-650 cathodes increases almost linearly with decreasing Li-ion content ($1 \leq x \leq 0.4$) in $Li_xNi_{0.94}Al_{0.06}O_2$. For the NA-675 and NA-700 cathodes, changes in parameter c as a function of state-of-charge (SOC) can be roughly divided into three regions: (1) slow increase in the SOC range of 0–30%, (2) fast increase between SOC values of 30% and 60%, (3) rapid fading in the SOC range from 60% to 85%. The difference between the maximum and minimum value of

parameter c for NA-675 and NA-700 cathodes is 4.12% and 4.59%, respectively, which are higher than that for NA-625 and NA-650 cathodes (2.92% and 2.78%). The c/a ratio, an indicator of trigonal distortion,[27] initially raises and then drops for all the electrodes during charging, demonstrating that the layered NA cathodes transform into a better-defined layered trigonal layered phase ($R\bar{3}m$) firstly and later become a more disordered layered phase as Li-ions are deintercalated from the layered structure. The unit-cell volume (V) for the electrodes decreases gradually until the delithiation degree reaches a value of about 0.40, and then declines quickly with the extraction of more Li-ions ($0.15 \leq x \leq 0.40$). The changes of these lattice parameters for all four electrodes are highly reversible upon relithiation, verifying a
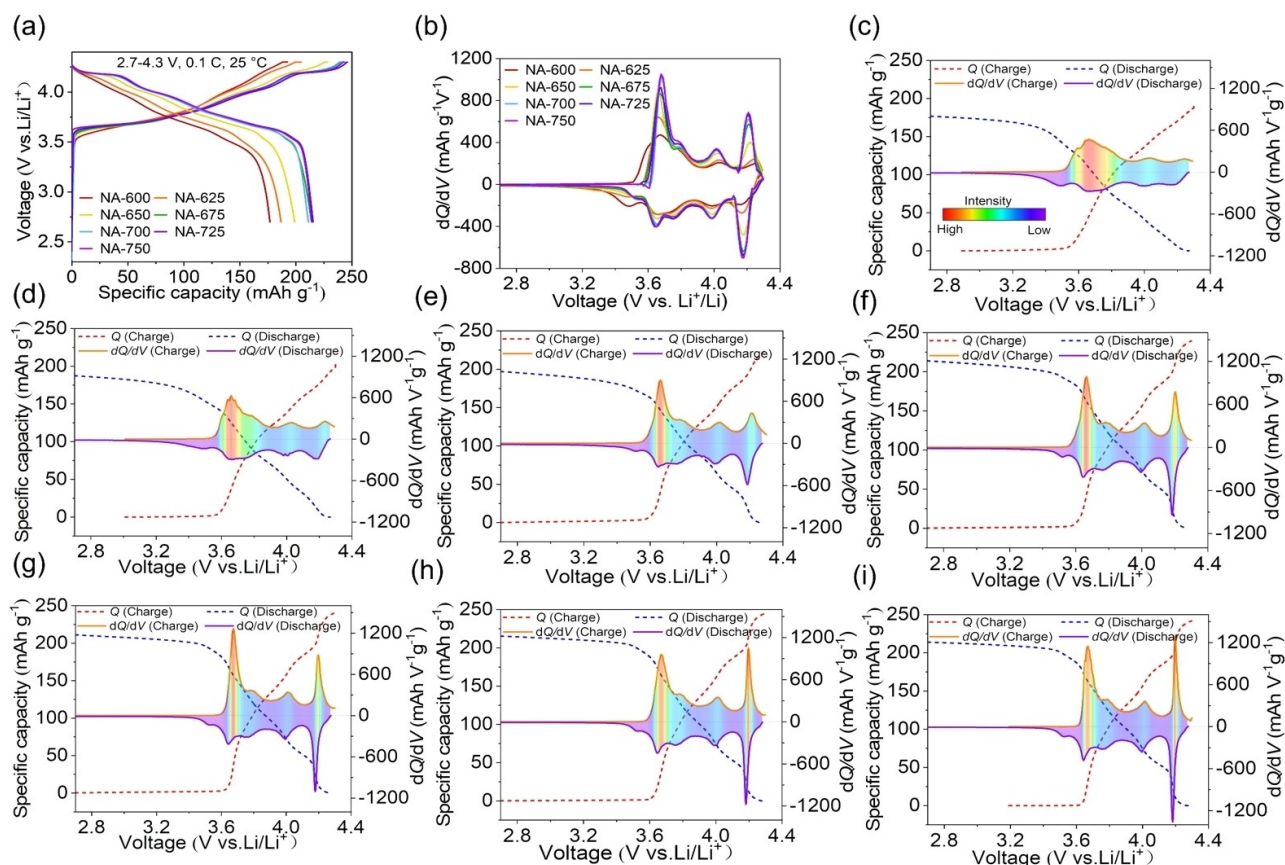
Figure 5. Electrochemical characteristics of NA cathodes. a) The first charge–discharge voltage profiles and b) the corresponding dQ/dV plots of NA electrodes; the initial charge–discharge potential curves and the dQ/dV profiles of c) NA-600, d) NA-625, e) NA-650, f) NA-675, g) NA-700, h) NA-725, and i) NA-750.

good structural stability. A significant change in the unit-cell volume of this layered structure during cycling would cause the formation of cracks along the secondary agglomerates, which would cause a loss of electrical contact between primary crystals and an increase of interfacial charge-transfer resistance, thus leading to inferior cycling performance.[1a,10,28] Therefore, a smaller reduction of unit-cell volume for the NA-650 electrode could be a major reason for the enhanced cyclic performance as shown in Figure 6e.

To determine whether the intergranular cracking caused structural fatigue and capacity fade during prolonged cycling, the morphological changes of NA electrodes were detected by SEM after 300 cycles at 1 C (Figure 9 and Figure S13–S14 Supporting Information). The morphology of NA agglomerates does not change considerably after long-term cycling. In contrast to the cycled NA-600 and NA-625 cathodes, both intergranular and intragranular cracks are visible in the other cycled electrodes owing to comparably large anisotropic lattice changes in these electrodes over cycling. It is interesting to point out that intergranular cracks can be observed in the inner region rather than on the surface of NA-625, which are possibly because of a comparably high interfacial strain between disoriented primary crystals in the core area of agglomerates.[29]

Considering that both NA-625 and NA-650 electrodes deliver an excellent cycling performance, thus, the capacity fade, especially for the 100 cycles at 1 C or 3 C, cannot be ascribed solely to intergranular cracking.

To figure out the main reason for structural degradation, XRD and TEM were conducted to investigate the long-range and local structural changes of NA electrodes during extended cycling. After 100 cycles at 1 C, obvious reflection broadening can be found in the NA-600 and NA-650 electrodes (Figure 10a, b and Figure S15, Supporting Information), revealing that the lattice dislocations or strains are successively generated in the long-range order after repeated Li deintercalation/intercalation.[16b] The broadening and weakening of 003 reflection for both electrodes become more pronounced with the increase of cycle number. In contrast, the fatigued NA-700 and NA-750 electrodes (Figure 10c, d and Figure S15, Supporting Information) display a clear phase segregation after 100 cycles, as evidenced by the splitting of the 003 reflection. Such phase segregation remains even after 300 cycles, illustrating a heterogeneous nature of NA-LCD cathodes. The main reflection in the XRD patterns of NA-700 and NA-750 electrodes at *d* value of ≈4.7 Å is supposed to be related to the active layered phase, whereas the broad and weak reflection at around 5.1 Å is attributed to the less reactive populations (i.e.
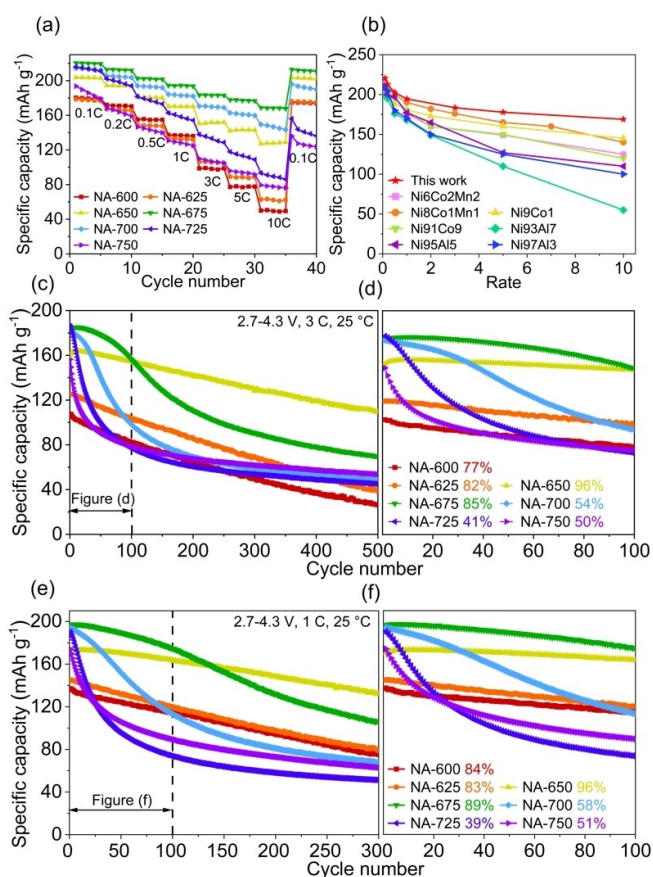
Figure 6. Electrochemical properties of NA cathodes between 2.7 and 4.3 V at 25 °C. a) Rate capabilities and c), d), e), f) cycling performances of NA electrodes; b) rate performance of NA-675 electrode compared to other high-Ni-content cathodes. The percentages in Figure (d) and (f) are the capacity retentions of NA cathodes after 100 cycles at 1 C and 3 C, respectively.

Figure 7. Structural evolution of NA cathodes during the first cycle. *In situ* XRD patterns of a) NA-625, b) NA-650, c) NA-675, and d) NA-700 electrodes, right figures display the corresponding charge–discharge voltage profiles; 3D maps of intensity and positions of 003 reflection for e) NA-620, f) NA-650, g) NA-675, and h) NA-700 electrodes, showing a solid solution reaction mechanism for these electrodes.

fatigue phase). It is worth mentioning that this fatigued phase cannot be indexed to the so-called rock-salt-type phase ($Fm\bar{3}m$), as demonstrated in numerous studies,[30] because the rock-salt structure does not produce any reflection over the *d* range between 4.0 and 5.0 Å. Instead, the additional weak reflections close to the main layered phase can still be assigned to a layered structure ($R\bar{3}m$), the fatigued phase is marked as a disordered layered phase in this work. The broadening of 003 reflection belonging to the disordered layered phase indicates a severe lattice distortion/mismatch along the *c*-axis.

Interestingly, distinct lattice distortions along the [001] direction are present in both inner and outer regions of the cycled NA-650 particles (Figure 10e–g), which matches precisely with the broadening of 003 reflection of the fatigued NA-650 electrode (Figure 10b). Thus, a slight capacity fade over extended cycling can be ascribed to a relatively high long-range cation mixing in NA-HCD electrodes because of the homogeneous degradation process (see Figure 11a), as evidenced by a good cycling performance of NA-625 and NA-650 electrodes. By contrast, there are no evident changes in the bulk lattice of the aged NA-
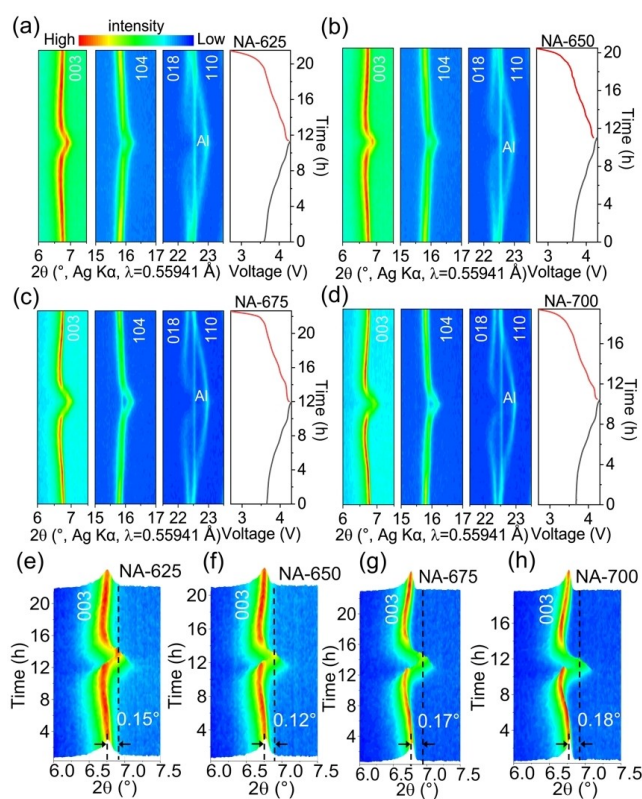
700 particles, while a discernibly larger spacing of 0.51 nm in the near surface area is probed with a clear disordered surface layer (Figure 10h–j), in excellent agreement with the fatigued phase in the XRD results (Figure 10c). These results provide direct evidence for phase segregation in a single crystallite, i.e. the formation of a "core–shell" structure (see Figure 11b). Although the fatigued phase on the surface is a disordered layered structure, it is still partially reactive due to the fact that the NA-700 electrode can still deliver a low capacity of ≈68 mAh g⁻¹ after 300 cycles at 1 C. The kinetic properties of NA-650 and NA-700 electrodes were investigated by impedance spectroscopy. The impedance data were collected after 1, 50, 100 and 300 cycles at 1 C, as depicted in Figure S16. The impedance spectra for both NA-650 and NA-700 cathodes are composed of a semicircle in the high frequency region, a semicircle in the medium frequency region and a low-frequency Warburg tail. Typically, the high-frequency arc represents the resistance of surface film (R_f), whereas the medium-frequency reflects the charge-transfer resistance (R_{ct}). Both ohmic resistance (R_b) and R_f do not increase considerably during cycling. The R_{ct} of the NA-650 electrode arises gradually from ≈20 Ω after 1 cycle to ≈460 Ω after 300 cycles. In contrast, noticeable growth of R_{ct} is clearly observed in the NA-700 electrode, i.e. from ≈26 Ω after
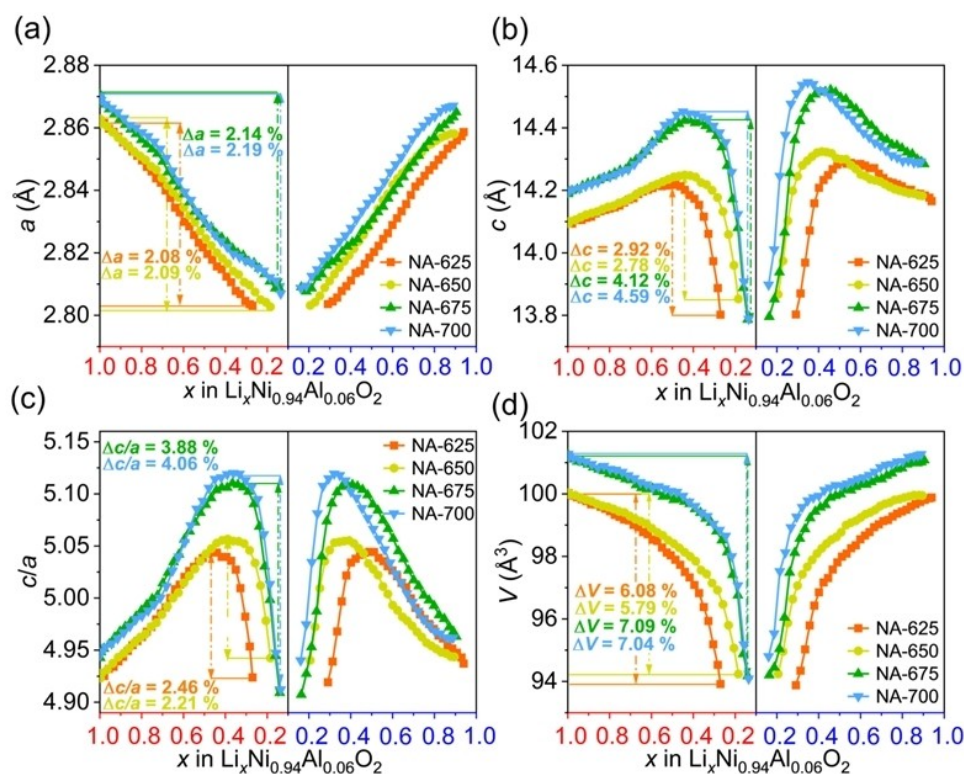
Figure 8. Variation of lattice parameters of NA cathodes during the first cycle. Changes of lattice parameter a) a, b) c and c) c/a, and d) unit-cell volume V of the electrodes during Li-ion extraction and insertion.
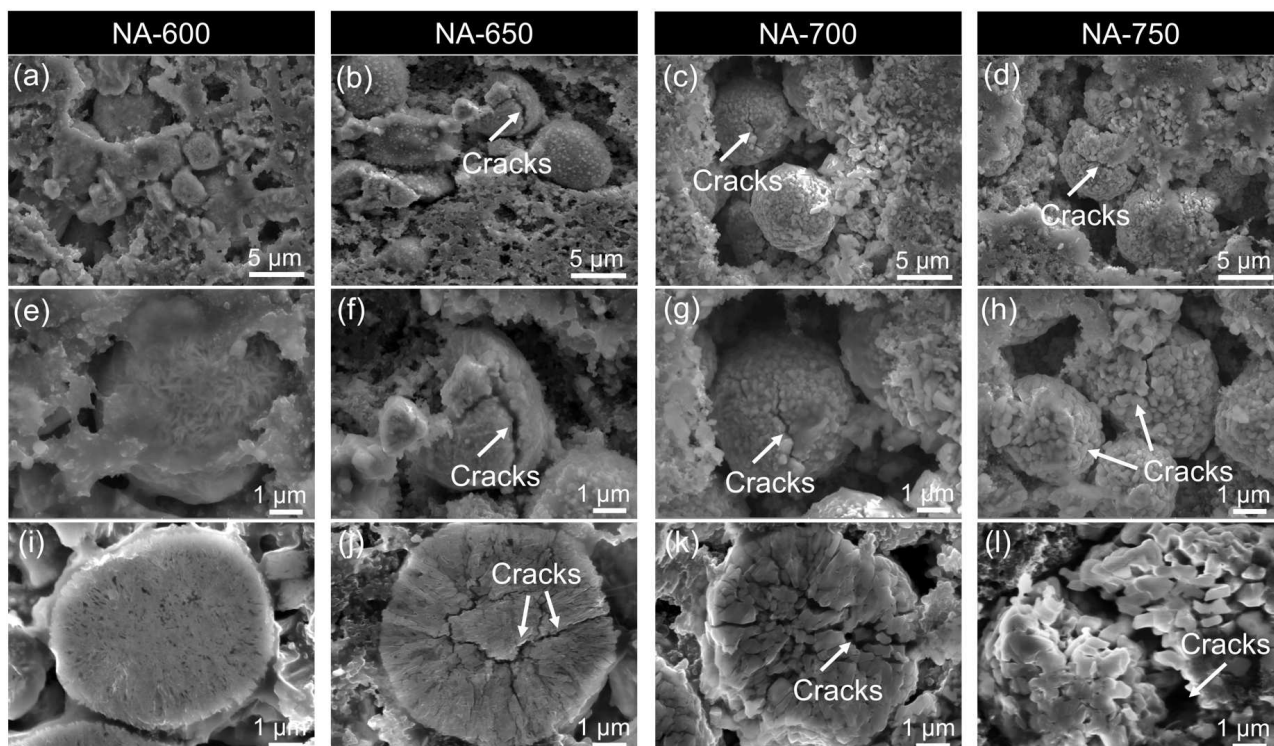

Figure 9. Observation of intergranular cracking in NA cathodes after 300 cycles at 1 C. SEM images of a), e) NA-600, b), f) NA-650, c), g) NA-700 and d), h) NA-750; cross-sectional SEM images of i) NA-600, j) NA-650, k) NA-700, l) NA-750.
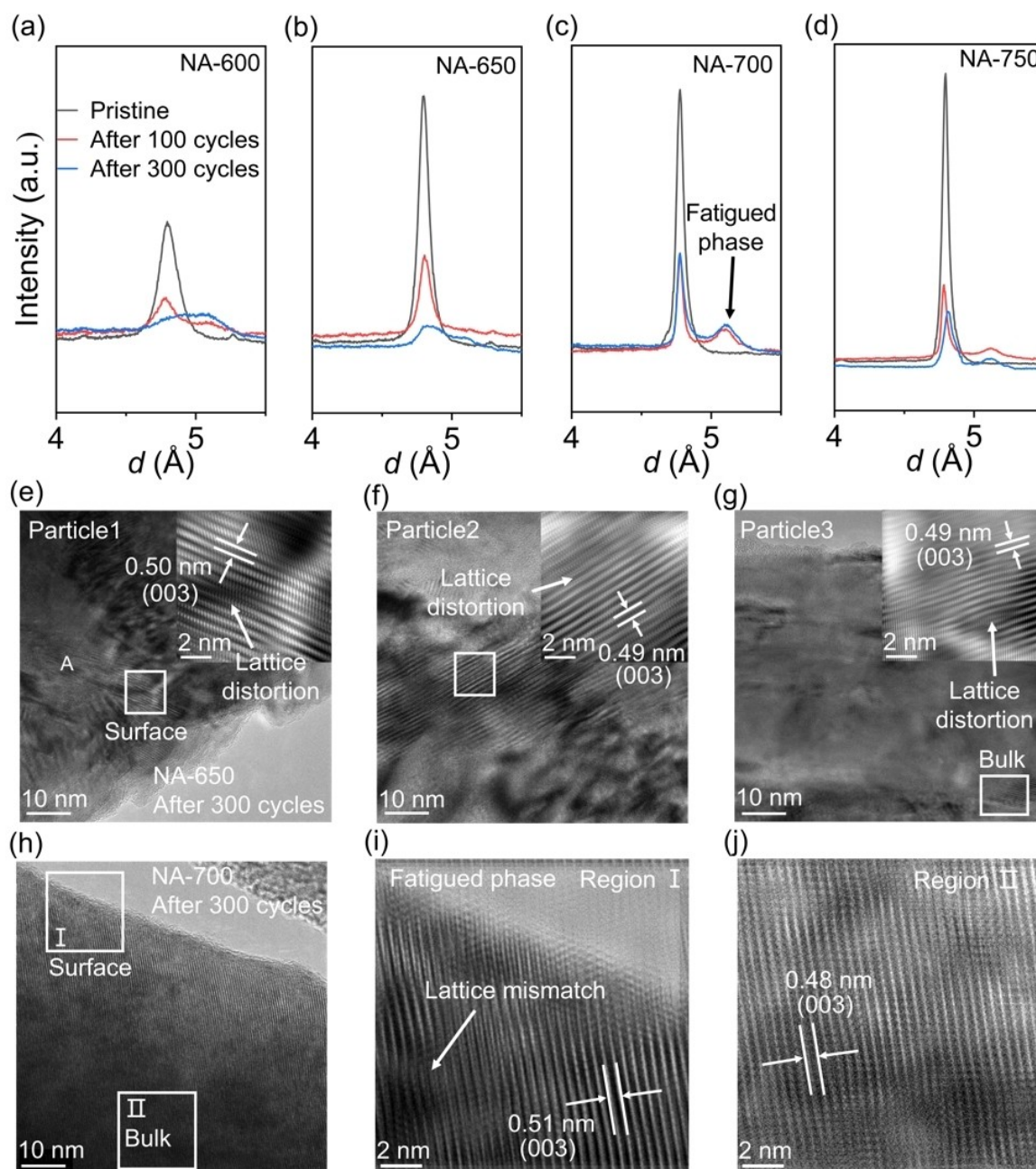
Figure 10. Post-mortem analysis of NA cathodes in the discharged state after long-term cycling. XRD patterns of a) NA-600, b) NA-650, c) NA-700 and d) NA-750 electrodes before cycling and after 100, 300 cycles at 1 C; HRTEM images and IFFT-TEM images (inset) of e), f), g) NA-650 electrodes after 300 cycles at 1 C; low-magnification HRTEM images of h) NA-700 electrodes after 300 cycles at 1 C; zoomed image of the fatigued NA-700 particle's i) bulk and j) surface.

1 cycle to $\approx 870\,\Omega$ after 100 cycles and further to $\approx 1190\,\Omega$ after 300 cycles. Such a large increase of charge-transfer resistance for the NA-700 electrode during the first 100 cycles can be ascribed to the disordered surface layer with lattice mismatch (i.e "core–shell" structure),[31] thus resulting in a rapid capacity fade of the NA-700 cathode for the first 100 cycles. The formation of the core–shell structure in NA-700 particles is most likely caused by their highly reactive surface.[30c] Comparably, a relatively high degree of Li/Ni disorder could create strong 180° Ni–O–Ni super

exchange chains in the near-surface region of crystallites, which contribute to the improvement in the stability of surface structure.[12b,32] As a consequence, NA-650 cathode experiences a homogeneous degradation pathway upon long-term cycling (see Figure 11). Since the degree of long-range cation disorder of the NA-700 cathode is similar to that of NA-725 and NA-750 cathodes, a faster capacity fading of NA-725 and NA-750 cathodes during initial 100 cycles is supposed to stem from their larger primary particles (>560 nm), compared to NA-700 (≈ 420 nm), that
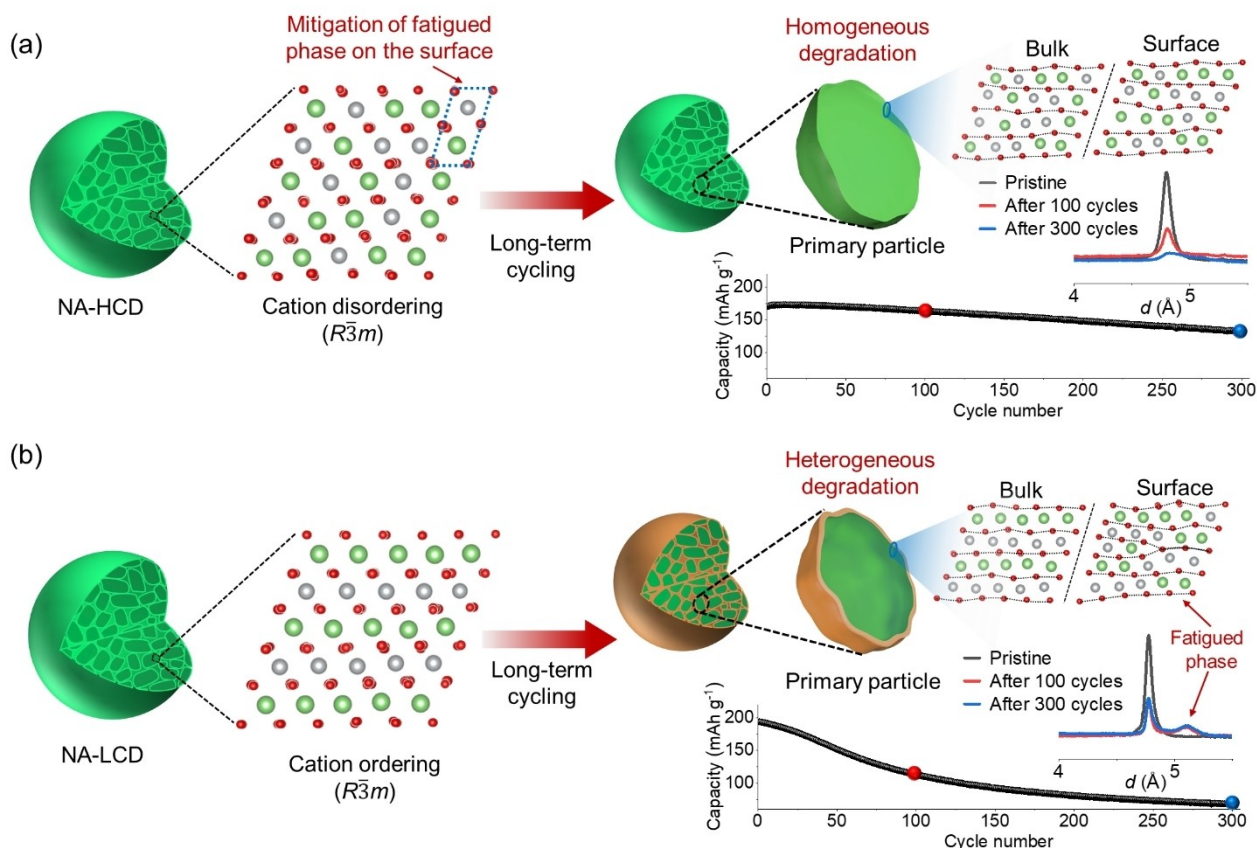
Figure 11. Schematic diagram of a) NA-HCD and b) NA-LCD degradation processes upon long-term cycling.

could trigger higher charge transfer resistance (see Figure S17 and Table S16). It should be noted that the primary particle size dose not increase significantly as the temperature reaches up to 675 °C. Therefore, the degree of initial long-range cation disorder is believed to be a major contribution to the different electrochemical activities of NA-HCD materials.

In order to find out whether the improved cycle performances of NA-HCD are attributed to their relatively low SOC compared to NA-LCD in a narrow voltage range of 2.7 to 4.3 V, the NA-650 and NA-750 electrodes were tested between 2.8 and 4.6 V (see Figure S18). The initial specific capacity of NA-650 cathode is 228 mAh g^{-1} at 0.1 C, which is close to that of NA-750 cathode (229 mAh g^{-1}). After 50 cycles at 0.5 C, the capacity retention of NA-650 and NA-750 electrodes is about 92 and 69 %, respectively, further demonstrating an enhanced cyclic stability and structural stability of NA-HCD. To clarify whether the uncovered degradation pathways during long-term cycling has broad implications for the design of a class of Co-free Ni-rich cathode materials, a series of layered Li(Ni$_{1-n}$Al$_n$)O$_2$ oxides with various compositions (n = 0.2, 0.1, 0.08, 0.04, 0.02 and 0.00) were synthesized by heating of hydroxide precursor and LiOH·H$_2$O at 650 or 750 °C. Correspondingly, the samples are labelled as NA20-650, NA20-750, NA10-650, ..., NA0-650 and NA0-750, respectively. All reflections of these samples can be indexed according to a rhombohe-

dral α-NaFeO$_2$ type layered structure ($R\bar{3}m$), as shown in Figure S19 and Figure S20. Rietveld refinement results suggest that the oxides obtained at 650 °C possess a higher degree of Li/Ni disorder when compared with the oxides prepared at 750 °C (Table S17). Figure S21 exhibits the cycling performance of these cathode materials at 3 C. Evidently, there is a rapid capacity fading in NA4-750, NA2-750 and NA0-750 cathodes upon cycling, whereas the NA4-650, NA2-650 and NA0-650 cathodes exhibit a superior cycle performance. The integrated intensity of 003 reflection decreases for cycled NA4-650 electrode after 100 cycles, while a weak reflection close to the 003 reflection appears in the XRD pattern of NA4-750 electrode. These results are comparable to the NA-650 and NA-700 electrodes (see Figure 6c, d), indicating that the Li(Ni$_{1-n}$Al$_n$)O$_2$ cathodes with low Al content ($n \leq 0.06$) display similar degradation pathways at a fast charge/discharge rate of 3 C. Noticeably, when the Al content is higher than 0.06 in Li(Ni$_{1-n}$Al$_n$)O$_2$, the discharge capacities of these materials with both low and high degree of cation disorder do not reduce rapidly as an increase in the number of cycles. These data suggest that the phase segregation in the near surface region of primary particles could be effectively mitigated via Al substitution during prolonged cycling. On the other hand, the discharge capacity of Li(Ni$_{1-n}$Al$_n$)O$_2$ cathodes decreases with increased amounts of substitution Al for Ni (Figure S21).

Therefore, the appropriate composition of $LiNi_{0.94}Al_{0.06}O_2$ was chosen in this study.

Conclusion

In conclusion, we show that the high-Ni-content cathode materials undergo two distinct degradation processes, which highly depend on the degree of long-range cationic disordering in the rhombohedral layered structure. The $Li_{1-m}(Ni_{0.94}Al_{0.06})_{1+m}O_2$ oxides with low cation disorder (NA-LCD, $x \leq 0.06$) is prone to the formation of "core–shell" structure (i.e. disordered surface with lattice mismatch), revealing the heterogeneous nature of NA-LCD electrodes. Such a "core–shell" structure is found to be a key contributor to the rapid capacity decay of NA-LCD electrodes during initial cycles. Although the NA-HCD cathodes deliver a relatively low capacity, they generally possess a good cyclic stability resulting from a comparably homogeneous fatigue process. The optimized NA-675 electrode exhibits competitive rate performance, e.g. a high discharge capacity of 169 mAh g^{-1} at 10 C. Besides, the experimental results demonstrate that the intergranular cracking and the increased Li/Ni cation mixing cannot be the primary origin of the structural degradation upon long-term cycling, although they have occurred in these Ni-rich materials. These findings provide not only significant and valuable information for engineering high-performance Ni-rich cathode materials, but also offer fundamental principles to develop effective countermeasures (such as site selective doping and self-protective coating) to mitigate the structural degradation of the state-of-the-art layered materials.

Acknowledgements

Conflict of Interest

The authors declare no conflict of interest.

Data Availability Statement

The data that support the findings of this study are available on request from the corresponding author. The data are not publicly available due to privacy or ethical restrictions.

[1] a) Y. Bi, J. Tao, Y. Wu, L. Li, Y. Xu, E. Hu, B. Wu, J. Hu, C. Wang, J.-G. Zhang, Y. Qi, J. Xiao, *Science* **2020**, *370*, 1313–1317; b) C. Xu, K. Marker, J. Lee, A. Mahadevegowda, P. J. Reeves, S. J. Day, M. F. Groh, S. P. Emge, C. Ducati, B. Layla Mehdi, C. C. Tang, C. P. Grey, *Nat. Mater.* **2021**, *20*, 84–92; c) D. Luo, H. X. Xie, F. L. Tan, X. K. Ding, J. X. Cui, X. Y. Xie, C. Y. Liu, Z. Lin, *Angew. Chem. Int. Ed.* **2022**, *61*, e61; *Angew. Chem.* **2022**, e202203698.

[2] A. Manthiram, *Nat. Commun.* **2020**, *11*, 1500.

[3] a) W. Hua, M. Chen, B. Schwarz, M. Knapp, M. Bruns, J. Barthel, X. Yang, F. Sigel, R. Azmi, A. Senyshyn, A. Missiul, L. Simonelli, M. Etter, S. Wang, X. Mu, A. Fiedler, J. R. Binder, X. Guo, S. Chou, B. Zhong, S. Indris, H. Ehrenberg, *Adv. Energy Mater.* **2019**, *9*, 1803094; b) D. S. Hall, R. Gauthier, A. Eldesoky, V. S. Murray, J. R. Dahn, *ACS Appl. Mater. Interfaces* **2019**, *11*, 14095–14100; c) J. B. Goodenough, Y. Kim, *Chem. Mater.* **2010**, *22*, 587–603; d) W. Hua, X. Yang, N. P. M. Casati, L. Liu, S. Wang, V. Baran, M. Knapp, H. Ehrenberg, S. Indris, *eScience* **2022**, *2*, 183–291.

[4] a) H. Hyun, K. Jeong, H. Hong, S. Seo, B. Koo, D. Lee, S. Choi, S. Jo, K. Jung, H. H. Cho, H. N. Han, T. J. Shin, J. Lim, *Adv. Mater.* **2021**, *33*, 2105337; b) W. Lee, S. Muhammad, T. Kim, H. Kim, E. Lee, M. Jeong, S. Son, J.-H. Ryou, W.-S. Yoon, *Adv. Energy Mater.* **2018**, *8*, 1701788.

[5] a) G. Zubi, R. Dufo-López, M. Carvalho, G. Pasaoglu, *Renewable Sustainable Energy Rev.* **2018**, *89*, 292–308; b) S. Landini, J. Leworthy, T. S. O'Donovan, *J. Energy Storage* **2019**, *25*, 100887.

[6] R. Schmuch, R. Wagner, G. Horpel, T. Placke, M. Winter, *Nat. Energy* **2018**, *3*, 267–278.

[7] a) H. Zhu, Y. Tang, K. M. Wiaderek, O. J. Borkiewicz, Y. Ren, J. Zhang, J. Ren, L. Fan, C. C. Li, D. Li, X. L. Wang, Q. Liu, *Nano Lett.* **2021**, *21*, 9997–10005; b) L. Qiu, Y. Song, M. K. Zhang, Y. H. Liu, Z. W. Yang, Z. G. Wu, H. Zhang, W. Xiang, Y. X. Liu, G. K. Wang, Y. Sun, J. Zhang, B. Zhang, X. D. Guo, *Adv. Energy Mater.* **2022**, *12*, 2200022.

[8] a) J. Kim, H. Cho, H. Y. Jeong, H. Ma, J. Lee, J. Hwang, M. Park, J. Cho, *Adv. Energy Mater.* **2017**, *7*, 1602559; b) L. Wang, X. Lei, T. Liu, A. Dai, D. Su, K. Amine, J. Lu, T. Wu, *Adv. Mater.* **2022**, *34*, 2200744.

[9] Y. Zou, G. Liu, K. Zhou, J. Zhang, T. Jiao, X. Zhang, Y. Yang, J. Zheng, *ACS Appl. Energy Mater.* **2021**, *4*, 11051–11061.

[10] T. Liu, L. Yu, J. Lu, T. Zhou, X. Huang, Z. Cai, A. Dai, J. Gim, Y. Ren, X. Xiao, M. V. Holt, Y. S. Chu, I. Arslan, J. Wen, K. Amine, *Nat. Commun.* **2021**, *12*, 6024.

[11] a) N. Ikeda, I. Konuma, H. B. Rajendra, T. Aida, N. Yabuuchi, *J. Mater. Chem. A* **2021**, *9*, 15963–15967; b) P. Kurzhals, F. Riewald, M. Bianchini, H. Sommer, H. A. Gasteiger, J. Janek, *J. Electrochem. Soc.* **2021**, *168*, 110518.

[12] a) W. Hua, B. Schwarz, R. Azmi, M. Müller, M. S. Dewi Darma, M. Knapp, A. Senyshyn, M. Heere, A. Missyul, L. Simonelli, J. R. Binder, S. Indris, H. Ehrenberg, *Nano Energy* **2020**, *78*, 105231; b) D. Kong, J. Hu, Z. Chen, K. Song, C. Li, M. Weng, M. Li, R. Wang, T. Liu, J. Liu, M. Zhang, Y. Xiao, F. Pan, *Adv. Energy Mater.* **2019**, *9*, 19001756.

[13] a) D. Luo, J. X. Cui, B. K. Zhang, J. M. Fan, P. Z. Liu, X. K. Ding, H. X. Xie, Z. H. Zhang, J. J. Guo, F. Pan, Z. Lin, *Adv. Funct. Mater.* **2021**, *31*, 2009310; b) L. G. Wang, T. C. Liu, T. P. Wu, J. Lu, *Nature* **2022**, *611*, 61–67.

[14] a) J. Zheng, Y. Ye, T. Liu, Y. Xiao, C. Wang, F. Wang, F. Pan, *Acc. Chem. Res.* **2019**, *52*, 2201–2209; b) E. Zhao, L. Fang, M. Chen, D. Chen, Q. Huang, Z. Hu, Q.-B. Yan, M. Wu, X. Xiao, *J. Mater. Chem. A* **2017**, *5*, 1679–1686.

[15] S. Wang, W. Hua, A. Missyul, M. S. D. Darma, A. Tayal, S. Indris, H. Ehrenberg, L. Liu, M. Knapp, *Adv. Funct. Mater.* **2021**, *31*, 2009949.

[16] a) M. Bianchini, A. Schiele, S. Schweidler, S. Sicolo, F. Fauth, E. Suard, S. Indris, A. Mazilkin, P. Nagel, S. Schuppler, M. Merz, P. Hartmann, T. Brezesinski, J. Janek, *Chem. Mater.* **2020**, *32*, 9211–9227; b) W. Hua, S. Wang, M. Knapp, S. J. Leake, A. Senyshyn, C. Richter, M. Yavuz, J. R. Binder, C. P. Grey, H. Ehrenberg, S. Indris, B. Schwarz, *Nat. Commun.* **2019**, *10*, 5365.

[17] H. Li, W. Hua, X. Liu-Théato, Q. Fu, M. Desmau, A. Missyul, M. Knapp, H. Ehrenberg, S. Indris, *Chem. Mater.* **2021**, *33*, 9546–9559.

[18] L. Ben, H. Yu, B. Chen, Y. Chen, Y. Gong, X. Yang, L. Gu, X. Huang, *ACS Appl. Mater. Interfaces* **2017**, *9*, 35463–35475.

[19] K. Kang, Y. S. Meng, J. Breger, C. P. Grey, G. Ceder, *Science* **2006**, *311*, 977–980.

[20] M. Bianchini, M. Roca-Ayats, P. Hartmann, T. Brezesinski, J. Janek, *Angew. Chem. Int. Ed.* **2019**, *58*, 10434–10458; *Angew. Chem.* **2019**, *131*, 10542–10569.

[21] T. Ye, Z. Li, H. Yan, Y. Ha, D. Zhang, C. Zhou, L. Wang, L. Li, Q. Xiang, *Adv. Energy Mater.* **2022**, *12*, 2201556.

[22] M. Yoon, Y. Dong, J. Hwang, J. Sung, H. Cha, K. Ahn, Y. Huang, S. J. Kang, J. Li, J. Cho, *Nat. Energy* **2021**, *6*, 362–371.

[23] F. Wu, N. Liu, L. Chen, Y. Su, G. Tan, L. Bao, Q. Zhang, Y. Lu, J. Wang, S. Chen, J. Tan, *Nano Energy* **2019**, *59*, 50–57.

[24] H. Yu, Y. Cao, L. Chen, Y. Hu, X. Duan, S. Dai, C. Li, H. Jiang, *Nat. Commun.* **2021**, *12*, 4564.

[25] H. Cao, F. Du, J. Adkins, Q. Zhou, H. Dai, P. Sun, D. Hu, J. Zheng, *Ceram. Int.* **2020**, *46*, 20050–20060.

[26] a) L. de Biasi, A. Schiele, M. Roca-Ayats, G. Garcia, T. Brezesinski, P. Hartmann, J. Janek, *ChemSusChem* **2019**, *12*, 2240–2250; b) C. Xu, P. J. Reeves, Q. Jacquet, C. P. Grey, *Adv. Energy Mater.* **2021**, *11*, 2003404.

[27] a) W. Hua, K. Wang, M. Knapp, B. Schwarz, S. Wang, H. Liu, J. Lai, M. Müller, A. Schökel, A. Missyul, D. Ferreira Sanchez, X. Guo, J. R. Binder, J. Xiong, S. Indris, H. Ehrenberg, *Chem. Mater.* **2020**, *32*, 4984–4997; b) J. Lai, J. Zhang, Z. Li, Y. Xiao, W. Hua, Z. Wu, Y. Chen, Y. Zhong, W. Xiang, X. Guo, *Chem. Commun.* **2020**, *56*, 4886–4889.

[28] X. H. Meng, T. Lin, H. Mao, J. L. Shi, H. Sheng, Y. G. Zou, M. Fan, K. Jiang, R. J. Xiao, D. Xiao, L. Gu, L. J. Wan, Y. G. Guo, *J. Am. Chem. Soc.* **2022**, *144*, 11338–11347.

[29] a) R. Lin, S. M. Bak, Y. Shin, R. Zhang, C. Wang, K. Kisslinger, M. Ge, X. Huang, Z. Shadike, A. Pattammattel, H. Yan, Y. Chu, J. Wu, W. Yang, M. S. Whittingham, H. L. Xin, X. Q. Yang, *Nat. Commun.* **2021**, *12*, 2350; b) X. P. Cheng, Y. H. Li, T. C. Cao, R. Wu, M. M. Wang, H. Liu, X. Q. Liu, J. X. Lu, Y. F. Zhang, *ACS Energy Lett.* **2021**, *6*, 1703–1710.

[30] a) Y. Ming, W. Xiang, L. Qiu, W. B. Hua, R. Li, Z. G. Wu, C. L. Xu, Y. C. Li, D. Wang, Y. X. Chen, B. H. Zhong, F. R. He, X. D. Guo, *ACS Appl. Mater. Interfaces* **2020**, *12*, 8146–8156; b) H. Kim, M. G. Kim, H. Y. Jeong, H. Nam, J. Cho, *Nano Lett.* **2015**, *15*, 2111–2119; c) L. de Biasi, B. Schwarz, T. Brezesinski, P. Hartmann, J. Janek, H. Ehrenberg, *Adv. Mater.* **2019**, *31*, 1900985.

[31] a) H. Yu, Y. Cao, L. Chen, Y. Hu, X. Duan, S. Dai, C. Li, H. Jiang, *Nat. Commun.* **2021**, *12*, 4564b) T. Wang, K. Ren, W. Xiao, W. Dong, H. Qiao, A. Duan, H. Pan, Y. Yang, H. Wang, *J. Phys. Chem. C* **2020**, *124*, 5600–5607.

[32] J. Zheng, T. Liu, Z. Hu, Y. Wei, X. Song, Y. Ren, W. Wang, M. Rao, Y. Lin, Z. Chen, J. Lu, C. Wang, K. Amine, F. Pan, *J. Am. Chem. Soc.* **2016**, *138*, 13326–13334.
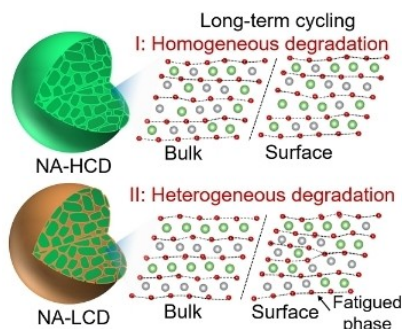
Research Articles

Li-Ion Batteries

W. Hua,* J. Zhang, S. Wang, Y. Cheng,
H. Li, J. Tseng, Z. Wu, C.-H. Shen,
O. Dolotko, H. Liu, S.-F. Hung, W. Tang,*
M. Li, M. Knapp, H. Ehrenberg, S. Indris,*
X. Guo* —————————— e202214880

Long-Range Cationic Disordering Induces
two Distinct Degradation Pathways in Co-
Free Ni-Rich Layered Cathodes

A series of Ni-rich $Li_{1-m}(Ni_{0.94}Al_{0.06})_{1+m}O_2$ (NA) oxides are synthesized through tailoring the heating temperature. The NA oxides with high cation disorder experience a comparably homogeneous fatigue process upon extended cycling, while a disordered surface with lattice mismatch is gradually formed in the NA with low cation disorder (i.e. heterogeneous degradation) which results in a rapid capacity decay during the fast charge–discharge cycling.